Nanoscale oxidation behavior of carbon fibers revealed with in situ gas cell STEM

Thomas J. Cochell,[†] Raymond R. Unocic,[‡] José Graña-Otero,[¶] and Alexandre Martin[*,¶]

[†]*Chemical & Materials Engineering, University of Kentucky, Lexington, KY*
[‡]*Center for Nanophase Materials Sciences, Oak Ridge National Laboratory, Oak Ridge, TN*
[¶]*Mechanical Engineering, University of Kentucky, Lexington, KY*

E-mail: alexandre.martin@uky.edu

Abstract

Thermal protection systems (TPS) are used to protect spacecraft payloads during the extreme conditions of atmospheric entry. The backbone of the composite TPS material used in the NASA Stardust Sample Return Capsule and the Mars 2020 mission is carbon fiber, which oxidizes at these temperatures and atmospheric conditions. This study presents the direct observation of carbon oxidation using *in situ* Scanning Transmission Electron Microscopy (STEM). A thin section of a commercially-available carbon fiber material containing multiple carbon structures was examined by STEM in a closed-environmental cell in which temperature was raised from 25 to 1050°C under a steady flow of air. Results show that the random polycrystalline carbon structure oxidized more uniformly and rapidly than the single crystallite region, which oxidized more anisotropically. These findings are the first to directly observe the structural dependence of carbon oxidation rates at these length-scales while also giving important insight into the onset of pitting at various active surface sites, important pieces in fundamentally understanding of carbon oxidation.

Keywords

Oxidation, *in situ* STEM, MEMS-based closed-cell gas, thermal protection systems TPS, ablation, carbon fibers

Introduction

Atmospheric entry spacecrafts are equipped with thermal protection systems (TPS) to shield the payload from extreme heating. The material used for TPS is usually a composite composed of a solid porous matrix and a polymer.[1] One such example is PICA[2] (phenolic-impregnated carbon ablator) which was used on the NASA Stardust Sample Return Capsule[3] as well as on the Mars Science Lab[4] and Mars 2020 entry vehicles.[5] PICA is a low-density, high-porosity ablative material made of a carbon fiber preform, FiberForm,® impregnated with phenolic resin. During the heating phase of the atmospheric entry, the phenolic rapidly pyrolyzes, with only the charred preform remaining.[6–10] The exposed carbon fibers interact with the oxygen in the atmosphere – or species containing oxygen, such as CO_2 – and start to oxidize. The ability of the charred carbon fibers to survive the harsh entry conditions is directly linked to the carbon oxidation rates at high temperature and under an oxygen-rich environment.

From a fundamental standpoint, the chemistry of carbon oxidation remains poorly understood. Decades of research, starting in the 1950's,[11] have yielded global models of carbon oxidation where all the elementary processes are lumped into a few global reactions. Other global models have been developed using chemical equilibrium assumptions, and were verified using high enthalpy experiments.[12] Detailed kinetic mechanisms, including molecular-scale processes, remain elusive despite recent efforts to bridge the gap between microscopic and empirical approaches.[13–18]

More recently, molecular beam experiments have been performed to provide a better understanding of the interaction between the hot carbon char and oxygen.[19,20] These experiments have led to the construction of a finite-rate kinetic model based on reaction probabilities.[21,22] Contrary to previous models which are largely based on empirical measurements,[23,24] all the individual rates are directly calculated from molecular beam data.

One important aspect of oxidation relates to the evolution of the carbon surface topology, the phenomenon generically called "pitting".[25–28] Past experimental studies have found that in certain conditions, oxidation does not occur uniformly but takes the form of pits or crater-like cavities, randomly scattered across the otherwise smooth carbon surface.[29–33] These pits initiate at atomic vacancies, defects, or basal plane carbon atoms,[33,34] eventually reaching the scale of the diameter of the fibers.[35] Hahn[34] observed that the frequency, size and initiation sites of the pits on highly oriented pyrolytic graphic (HOPG) varies with temperature. At temperatures of less than 875°C, pits were only initiated by defects, while at higher temperatures, they were also initiated from basal plane layers.

Over the years, two main techniques have been used to perform *in situ* environmental transmission electron microscope (TEM) studies. The first method involves directly introducing gas in the high-vacuum column of a dedicated environmental TEM (ETEM).[36–38] However, this method severely limits the partial pressure of the reactive gas, as the column must remains at very low pressure. Moreover, the method is not without risks as the TEM column can be contaminated with the reactive gases. A more recent approach makes use of a specially designed closed cell gas reaction gas-cell holder.[39–44] With this method, the sample is contained within electron transparent silicon nitride membranes and the temperature, pressure and gas environment is controlled. The environment within the gas cell can be controlled by setting: a static gas quantity or gas flow, the temperature from ambient up to 1000°C and the pressure up to 1 atm. Additionally, the layer of gas in the cell is thin, thereby maintaining high spatial resolution.[45]

The surface roughness due to pitting affects the reactive area of the material, and therefore, the net oxidation rate. The current state-of-the-art resorts to *ad hoc* models of surface evolution.[46] Since the onset and propagation of this phenomenon is not fully understood, it is difficult to accurately predict the available reactive area or the oxidation rate. A better understanding of the evolution of pitting on a much smaller length scale is thus needed. The goal of this work is to study the oxidization of carbon at the microstructural-level. Previous work[35,47] has determined the bulk properties of FiberForm during oxidation in air, O_2 and CO_2. The current work builds on that to illuminate the microstructural-dependent properties of FiberForm and carbon such as the mechanism of pitting as opposed to the bulk properties such as mass loss and recession at given temperatures and reactant flow rates in previous work.[35] To this end, a thin section of FiberForm® was heated in a closed gas-cell under a steady flow of air while being examined in real-time using a scanning transmission electron microscope (STEM).

Results

Characterization of Carbon Fiber

A carbon specimen was sectioned from a carbon fiber within a sample of FiberForm and then thinned, using focused ion beam (FIB) techniques. The sample, taken from the interior of the fiber, was parallel to the longitudinal axis of the fiber, as shown in Fig. 1. The interior section specimen was then transferred to the top window of an Atmosphere E-chip as shown in the SEM image in the rightmost panel of Fig. 1 and hereafter called "FF-IS". The E-chip was sealed and held at a pressure of 76 torr with a small flow of air supplied throughout the experiment. The chip was resistively heated at 10°C/s in 50°C steps followed by isothermal holds for ∼10 min. Annular dark-field STEM images were acquired over the course of the experiment as shown in Fig. 2. Region 1, highlighted by the red box in Fig. 2(a), corresponds to the top portion of the specimen shown in the SEM image in Fig. 1, and is characterized by a uniform appearance. This region is shown to be uniform in thickness, based upon imaging with STEM and SEM. The dark region below Region 1, labeled "Background" in Fig. 2(a), is the electron transparent Si_xN_y window on the E-chip shown in Fig. 1. Region 2, shown by the green box in Fig. 2(a), corresponds to the ∼1 μm strip of material running across the specimen and parallel to the fiber axis. This structure is also apparent in the SEM image in Fig. 1 and is characterized by a more heterogeneous micro-structure with what appears to be inclusions and voids.

Multiple studies have shown the presence of microvoids or pores in both polyacrylonitrile-based (PAN) and mesophase pitch-based carbon fibers.[48–53] Guigon et al.[52] attributes the irregular pores to the void space between the crumbled sheets of carbon similar to what would happen when crumpling a sheet of paper. Qin et al.[48] attributed microvoids on the surface and interior of PAN-based carbon fibers to the release of nitrogen and the rearrangement of crystallite during high-temperature heat treatments. Other studies[51,53] point to needle-shaped voids that can been seen using TEM but were first proposed by Perret and Ruland[54]. Perret and Ruland[54] attributes these needle-shaped voids to the non-ideal stacking of the microfibrils of carbon such that the space between these nearly parallel stacked ribbons is not completely filled. Due to the relatively large size of the voids shown in Figs. 1 and 2, and the many crystallites seen in Region 2, it seems most likely that these voids are due to the rearrangement of crystallites during a heat treatment similar to what is described by Qin et al.[48]. Since the specimen was thinned to a relatively uniform thickness using FIB, the contrast differences between Regions 1 and 2 are assumed to be due to diffraction effects and density differences.

The major finding from the reported experiment is the different oxidation behaviors observed by the two significantly different microstructural regions: Region 1 and 2. Based on the stark differences in appearance of Regions 1 and 2, High-resolution TEM (HRTEM) was performed on the specimen and similarly structured carbon fiber sections to study the differences. HRTEM prior to oxidation confirmed that the structure of the two regions is in fact very different. Fig. 3 shows HRTEM images of a similar structured FiberForm specimen where the center section contains inclusions – like Region 2 in FF-IS – and is surrounded by a uniform region – like Region 1 in FF-IS. The continuous and wavy lattice fringes of the

(002) crystallographic planes are running vertically in the top inset of Fig. 3, indicative of the inclusions being large single crystallites. In this particular crystallite, shown in Fig. 3, the basal planes stack laterally along the larger image. Needle-shaped voids oriented vertically and parallel with the lattice fringes can also be seen in Fig. 3. More detailed images are included in the Supporting Information (Fig. 5) and show these voids to be between ribbons in the structure close to where the carbon folds over on itself, which is strikingly similar to the mechanism proposed by Perret and Ruland[54]. Based on the structure in Fig. 3 and the appearance of the inclusion marked by the green cross in Fig. 2(a), it is concluded that the basal planes stack approximately normal to the image.

The wavy pattern has been seen in the lattice fringes of many studies on PAN-based carbon fibers as pointed out in the review by Edie[55]. The appearance is proposed to be from the interlinked turbostratic layers of carbon present in the precursor PAN fibers that have a fibril structure.[55] A measurement of multiple lattice fringes shows that the d-spacing is 0.38 nm, which is significantly larger than the (002) plane spacing of graphitic carbon, 0.34 nm. Edie[55] reported that multiple studies on carbon fibers have observed interlayer spacings larger than those of graphite with a d-spacing of 0.38 nm being within the range of values reported by Bennett and Johnson[53]. It should be noted that this microstructure is generally attributed to the “skin” of carbon fibers, which does not seem to be the case here since Region 2 occurs in the fiber interior and is thicker than the skin regions commonly reported. However, Region 2 does have similar characteristics such as the highly aligned large crystallites. It should be noted that there is a subtle line running along the bottom of FF-IS parallel to the fiber axis shown in Fig. 1. This line is located ∼400 nm from the exterior surface of the FiberForm, and may represent the transition between skin and core regions discussed in the literature. For example, Frank et al.[51] showed a dark-field TEM image of a 6-7 μm diameter PAN-based carbon fiber with a skin region that is 150-250 nm thick. The structure of Region 1 in Fig. 2, on the other hand, is the same as the lower inset in Fig. 3, which appears to be much more disordered with only small regions of lattice fringes visible and at random orientations to one another. This structure resembles the core region of a PAN-based carbon fiber proposed by Johnson[56] in which the structural organization in cross section is random due to the extensive folding of the core layer planes. More HRTEM images can be found in the Supporting Information documents (Fig. 5), showing more detailed views of the needle-shaped voids and sheet folding present in these fibers.

Based on the random structure exposed during the FIB process (Region 1), it was expected that numerous active surface sites would be available for O_2 during oxidation. This would result in uniform and rapid oxidation normal to the surface of the carbon. On the other hand, the highly ordered structure of the inclusions in Region 2 would mean far fewer active surface sites, and results in slower, more directional oxidation from the edges of the basal planes and defects. Since sites other than basal plane edge sites and defects do not favor oxidation,[57] oxidation normal to the basal plane would be much lower than lateral oxidation, and would strongly dependent on surface defects. Both of these predictions are verified by the oxidation experiment.

Oxidation of Carbon Fiber

The grey-scale values in the regions discussed above were analyzed over the course of the experiment to quantify the oxidation of the carbon microstructures. Fig. 4(a) shows the percentage of the original grey-scale value averaged over the entire Region 1, and the center of the inclusion particle in Region 2, marked by a green cross. To account for image variabilities, those values were normalized by the background value of the window in the FF-IS chip. This method provides an approximation of the relative thickness of the FiberForm specimen as long as the grey-scale of the background remains constant. Jonge et al.[58] used a similar approach to calculate the thickness of gold nanoparticles in a STEM liquid flow-cell. They used a Rutherford scattering approach to model the elastic scattering of electrons in ADF imaging mode, which they use to compare the thickness of gold nanoparticles against known values. Sacci et al.[59] used this approach to identify lithium-containing deposits formed during potential sweeping of a model Li-ion battery system in a liquid-cell STEM experiment.

The background grey-scale value of FF-IS remains constant until 70 min (or 950°C) into the experiment at which point (Figs. 2(i) to 2(l)) the $\mathrm{Si_xN_y}$ window becomes heterogeneous in brightness, with lighter spots forming. A lighter spot in ADF mode indicates an increase in thickness or an increase in density. SEM images from another FiberForm specimen and E-chip, taken before and after a similar oxidation experiment, show that only the $\mathrm{Si_xN_y}$ window with a FiberForm specimen on top undergoes noticeable differences in appearance (Fig. 6 of the Supporting Information), suggesting that the change is the result of deposition of oxidation products or tungsten impurities from the FIB transfer procedure and not an oxidation of the $\mathrm{Si_xN_y}$ material. Post-mortem images of FF-IS were not taken due to extensive oxidation to the carbon specimen.

Fig. 4(a) shows that the greyscale of all regions did not change noticeably until a temperature of 750-800°C was reached, indicating that the specimen thickness remains essentially the same and little oxidation occured. By the time the temperature rose to 900°C, the greyscale value of Region 1 was still 80% of the original value, having decreased by 2 percentage points per minute (pp/min) or less. The greyscale value decreased at a rate of 3 pp/min ($R^2 = 0.88$) during the isothermal hold at 900°C, and then the rate increased to 7 pp/min ($R^2 = 0.97$) at 950°C until the background level changed. At this point the greyscale value of Region 1 leveled off, even increasing slightly. This is likely due to the changes of the $\mathrm{Si_xN_y}$ window that occurs at 70.0 min, but may also be a result of the appearance of small white spots in Region 1 (Fig. 2(i) to 2(l)). A previous study utilizing energy dispersive X-ray spectroscopy (EDS) by Panerai et al.[47] found these white spots to be rich in calcium and oxygen, with trace amounts of silicon, sodium, sulfur and potassium. X-ray diffraction (XRD) of the white residue left from oxidizing FiberForm in a conventional furnace showed these white deposits to be a mixture of calcium oxide and calcium silicate (Fig. 7 of the Supporting Information). These calcium- and silicon-rich particles could be responsible for the change to the $\mathrm{Si_xN_y}$ window.

Examining Fig. 2 shows that Region 1 started to darken in ADF mode at ∼750°C and continued to darken with increasing time/temperature, indicative of uniform thinning of the region. Brightness in ADF mode of STEM imaging is proportional to atomic number and thickness. Therefore if the image is darkening with no composition changes, then the thickness is decreasing. However, the behavior observed in Region 2 is different than that in Region 1. For one, thinning of Region 2 is not uniform. As can be seen in the square inclusion in Fig. 2 in which the grey-scale decreases from the outside of the particle inward. This behavior is consistent with lateral oxidation from the edges of basal plane layers and stacking of basal planes normal to the image. The onset of oxidation at the edges of the inclusion shown in Region 2 of Fig. 2 is similar to Region 1 as can be seen by comparing Fig. 4(b) with Fig. 4(a) and consistent with the temperature Hahn[34] reports for pitting initiated from basal plane layers. From Fig. 4(a), the grey-scale value of the center of the inclusion remains very stable until the temperature reaches 1050°C, indicating that substantial oxidation is not occurring at the inclusion center until that temperature is reached. Additionally, if only considering the square inclusion in Fig. 2, the anisotropic oxidation extends to the vertical and horizontal dimensions of the particle as shown in Fig. 4(b). As defined in Fig. 4(b), the vertical and horizontal directions of the square inclusion begin noticeable reductions at ∼ 850°C. Above 850°C, the rate of vertical reduction is greater than the horizontal reduction indicating that the oxidation rate is more rapid in the vertical direction. Since the vertical and horizontal directions in Fig. 4(b) are orthogonal and the a-axes in the basal plane of carbon are at 60° to each other, this would explain the reported differences in rate along directions 90° from each other. It is not known with certainty however what crystallographic directions are parallel to the vertical and horizontal directions. This preferential oxidation within the basal plane of carbon has been observed in HOPG using scanning tunneling microscopy (STM) by the appearance of hexagonal pits once the pits reached a certain sizes.[33,60]

The results shown in Fig. 4(a) correlates to the meso-scale study of Panerai et al.[35]. In that experiment, a 20 mm thick sample of FiberForm was oxidized for 10 min in a quartz tube of flowing oxygen, at temperatures ranging from 200 to 1100°C. The results show that the sample remains non-reactive until a temperature of $\approx$ 500°C is reached, at which point a sudden mass loss is observed. The mass loss steadily increases with increasing temperature up to $\approx$ 1000°C where another steep increase is noted. Analysis of the product gas composition showed that the change in slope corresponds to an increase in CO and decrease in CO_2 following a Boudouard reaction at temperatures above $\sim$800°C. The current results did not show a significant decrease in thickness until 750-800°C. This could be due to differences in flow rates or flow conditions. In the flow tube experiment, gas is forced to flow through the porous FiberForm that is pressured fit within the tube, while the same is not true for the flow within the E-chip. The onset of thickness decrease shown in Fig. 4(a) does correspond to the temperature in Panerai et al.[35] at which point significant amounts of CO are observed. This suggests that the decrease in thickness is attributed to oxidation of carbon to produce mostly CO and that in this study minimal oxidation was observed in the temperature range in which a majority of CO_2 is produced. The significant mass loss and recession rates at temperatures as low as 400°C in Panerai et al.[35] would also suggest that bulk FiberForm is more closely related to Region 1 in the current study, whereas more ordered inclusions may only be present in small amounts.

One last observation to point out pertains to the potential "skin" region described above. While the subtle line can be seen in Fig. 1, it cannot be resolved prior to the oxidation experiment in ADF STEM (Fig. 2(a)). However, at 700°C a line parallel to the fiber axis can be seen developing at the bottom of FF-IS in the same location as the subtle line was seen in SEM. The development of this line could be the result of delamination during heating or lateral oxidation at basal plane edges. Interestingly, this edge region remains brighter than the surrounding Region 1 throughout the rest of the oxidation experiment (Fig. 2(e-l)) suggesting more similarities to the oxidation mechanism of Region 2 than Region 1. This would support the notion that this edge region is in fact the skin region.

In summary, different microstructures of a thin carbon fiber specimen were characterized and exhibited many similarities to PAN-based carbon fibers reported in the literature. These carbon microstructures showed unique oxidation behavior at temperatures ranging from 25-1050°C as observed using *in situ* TEM in a closed-environmental cell. These direct observations of carbon oxidation suggest the microstructural-dependent oxidation mechanisms proposed above to be true for Regions 1 and 2. These results provide further insight into the oxidation mechanisms of carbon fibers at the microstructure-level using *in situ* gas-cell STEM. The microstructural-dependent oxidation results provided by this state-of-the-art technique add to what our group has already reported about bulk oxidation of these carbon fiber materials in flow-tube experiments.[35,47] These insights allow for the design of advance TPS architectures and development of novel materials for future space missions.

Materials and Methods

As-received FiberForm® (Fiber Materials, Inc., Biddeford, ME, USA) was sectioned and thinned for imaging using a Hitachi NB5000 dual-beam focused-ion beam (FIB). A Protochips Atmosphere 200™(Morrisville, NC, USA) was used to study the oxidative behavior of FiberForm. FIB prepared FiberForm samples were transferred onto the $\mathrm{Si_xN_y}$ window of an Atmosphere E-chip while also being in physical contact with the SiC surrounding the window to enable resistive heating during the experiment. The E-chip was then installed into the Atmosphere holder according to the manufacturer's specifications creating a gas-tight seal that was verified in a vacuum chamber up to 1×10^{-6} mbar. Ar and O_2 (Ultra-high purity, Airgas) gases were supplied to the E-chip through the included gas manifold. The system was set for gas flow and air was constantly supplied throughout testing at a constant pressure of 76 torr. More experimental details on the use of the Protochips Atmosphere setup for studying closed-cell high-temperature gas reactions can be found in Unocic et al.[44]. *In situ* imaging was simultaneously captured in bright-field (BF) and annular dark-field (ADF) imaging modes using an FEI Titan S aberration-corrected STEM operating at 300 kV, in the Center for Nanophase Materials Sciences at Oak Ridge National Laboratory. Videos of the experiment were collected using Camtasia, a screen capture software, while continuously scanning the specimen. High-resolution TEM (HRTEM) imaging was conducting before and after the experiment using the FEI Titan along with additional post-mortem imaging taken by the dual-beam.

Acknowledgments

The authors thank D. Coffey (Oak Ridge National Laboratory) for her expert FIB specimen preparation and useful discussions, N. Briot (Electron Microscopy Center, University of Kentucky) for his help in preparing the samples as well as T. Dolan (College of Medicine, University of Kentucky) for his illustrations. This research was supported in part by a grant from the Kentucky Science and Engineering Foundation as per Grant/Award Agreement KSEF-3939-RDE-020 with the Kentucky Science and Technology Corporation, as well as from NASA Space Technology Research Grants Program, Early Stage Innovations (ESI) award NNX15AD73G. *In situ* STEM experiments and HRTEM imaging were conducted at the Center for Nanophase Materials Sciences, which is a DOE Office of Science User Facility.

References

(1) Bowman, W. H.; Lawrence, R. M. *Journal of Chemical Education* **1971**, *48*, 690–691.

(2) Tran, H. K.; Johnson, C. E.; Rasky, D. J.; Hui, F. C. L.; Hsu, M. T.; Chen, T.; Chen, Y.-K.; Paragas, D.; Kobayashi, L. *Phenolic Impregnated Carbon Ablators (PICA) as Thermal Protection Systems for Discovery Missions*; Technical Report NASA-TM-110440, 1997.

(3) Kontinos, D. A.; Wright, M. J. *Journal of Spacecraft and Rockets* **2010**, *47*, 705–707.

(4) *Nature* **2011**, *479*, 446–446.

(5) Hwang, H.; Bose, D.; Wright, H.; White, T. R.; Schoenenberger, M.; Santos, J.; Karlgaard, C. D.; Kuhl, C.; Oishi, T.; Trombetta, D. Mars 2020 Entry, Descent, and Landing Instrumentation (MEDLI2). 46th AIAA Thermophysics Conference. 2016.

(6) Weng, H.; Duzel, U.; Fu, R.; Martin, A. *Journal of Spacecraft and Rockets* **2020**, Accepted (Manuscript ID 2019-07-A34828).

(7) Weng, H.; Martin, A. *Journal of Thermophysics and Heat Transfer* **2015**, *29*, 429–438.

(8) Weng, H.; Bailey, S. C. C.; Martin, A. *International Journal of Heat and Mass Transfer* **2015**, *80*, 570–596.

(9) Weng, H.; Martin, A. *Journal of Thermophysics and Heat Transfer* **2014**, *28*, 583–597.

(10) Omidy, A. D.; Panerai, F.; Lachaud, J. R.; Mansour, N. N.; Martin, A. *Journal of Thermophysics and Heat Transfer* **2016**, *30*, 472–477.

(11) Walker, P. L.; Rusinko, F.; Austin, L. G. In *Advances in Catalysis*; Eley, D. D., Selwood, P. W., Weisz, P. B., Eds.; Academic Press, 1959; Vol. 11; pp 133–221.

(12) Milos, F. S.; Gasch, M. J.; Prabhu, D. K. *Journal of Spacecraft and Rockets* **2015**, *52*, 804–812.

(13) Campbell, P.; Mitchell, R. *The impact of the distributions of surface oxides and their migration on characterization of the heterogeneous carbon–oxygen reaction*; 2008; Vol. 154; pp 47–66.

(14) Du, Z.; Sarofim, A. F.; Longwell, J. P.; Mims, C. A. *Energy and Fuels* **1991**, *5*, 214–221.

(15) Geier, M.; Shaddix, C.; Holzleithner, F. *A mechanistic char oxidation model consistent with observed CO2/CO production ratios*; 2013; Vol. 34; p 2411.

(16) Haynes, B. S. *Combustion and Flame* **2001**, *126*, 1421–1432.

(17) Hurt, R. H.; Calo, J. M. **2001**,

(18) Mitchell, R.; Ma, L.; Kim, B. *On the burning behavior of pulverized coal chars*; 2007; Vol. 151; pp 426–436.

(19) Paci, J. T.; Upadhyaya, H. P.; Zhang, J.; Schatz, G. C.; Minton, T. K. *Journal of Physical Chemistry A* **2009**, *113*, 4677–4685.

(20) Murray, V. J.; Marshall, B. C.; Woodburn, P. J.; Minton, T. K. *Journal of Physical Chemistry C* **2015**, *119*, 14,780–14,796.

(21) Poovathingal, S.; Schwartzentruber, T. E.; Murray, V. J.; Minton, T. K. *AIAA Journal* **2016**, *54*, 1–11.

(22) Poovathingal, S.; Schwartzentruber, T. E.; Murray, V. J.; Minton, T. K.; Candler, G. V. *AIAA Journal* **2017**, 1–15.

(23) Park, C. *AIAA Journal* **1976**, *14*, 1640–1642.

(24) Zhluktov, S. V.; Abe, T. *Journal of Thermophysics and Heat Transfer* **1999**, *13*, 50–59.

(25) Nicholson, K. T.; Minton, T. K.; Sibener, S. J. *The Journal of Physical Chemistry B* **2005**, *109*, 8476–8480.

(26) Panerai, F.; Martin, A.; Mansour, N. N.; Sepka, S. A.; Lachaud, J. *Journal of Thermophysics and Heat Transfer* **2014**, *28*, 181–190.

(27) Stevens, F.; Kolodny, L. A.; Beebe, T. P. *The Journal of Physical Chemistry B* **1998**, *102*, 10799–10804.

(28) Levet, C.; Helber, B.; Couzi, J.; Mathiaud, J.; Gouriet, J.-B.; Chazot, O.; Vignoles, G. *Carbon* **2017**, *114*, 84–97.

(29) Helber, B.; Chazot, O.; Magin, T.; Hubin, A. Ablation of Carbon Preform in the VKI Plasmatron. 43$^{\mathrm{rd}}$ AIAA Thermophysics Conference. New Orleans, LA, USA, 2012.

(30) Helber, B.; Chazot, O.; Hubin, A.; Magin, T. E. *Journal of Visualized Experiments* **2015**,

(31) Helber, B.; Chazot, O.; Hubin, A.; Magin, T. E. *Composites Part A: Applied Science and Manufacturing* **2015**, *72*, 96–107.

(32) Miller-Oana, M. Oxidation Behavior of Carbon and Ultra-High Temperature Ceramics. Ph.D. thesis, University of Arizona, Tucson, AZ, 2016.

(33) Chang, H.; Bard, A. J. *Journal of the American Chemical Society* **1991**, *113*, 5588–5596.

(34) Hahn, J. *Carbon* **2005**, *43*, 1506 – 1511.

(35) Panerai, F.; Cochell, T. J.; Martin, A.; White, J. D. *International Journal of Heat and Mass Transfer* **2019**, *136*, 972–986.

(36) Wang, C.-M.; Genc, A.; Cheng, H.; Pullan, L.; Baer, D. R.; Bruemmer, S. M. *Scientific Reports* **2014**, *4*, Article number 3683.

(37) Wang, C.-M.; Schreiber, D. K.; Olszta, M. J.; Baer, D. R.; Bruemmer, S. M. *ACS Applied Materials and Interfaces* **2015**, *7*, 17272–17277.

(38) Jeangros, Q.; Hansen, T. W.; Wagner, J. B.; Dunin-Borkowski, R. E.; Hebert, C.; Hessler-Wyser, J.; Hébert, C.; herle, J. V.; Hessler-Wyser, A. *Acta materialia* **2014**, *67*, 362–372.

(39) Allard, L. F.; Bigelow, W. C.; Overbury, S. H.; Nackashi, D. P.; Damiano, J. *Microscopy and Microanalysis* **2010**, *16*, 296–297.

(40) Allard, L. F.; Overbury, S. H.; Bigelow, W. C.; Katz, M. B.; Nackashi, D. P.; Damiano, J. *Microscopy and Microanalysis* **2012**, *18*, 656–666.

(41) Allard, L.; Overbury, S.; Katz, M.; Bigelow, W.; Nackashi, D.; Damiano, J. *Microscopy and Microanalysis* **2012**, *18*, 1118–1119.

(42) Allard, L. F.; Bigelow, W. C.; Zhang, S.; Pan, X.; Wu, Z.; Overbury, S. H.; Carpenter, W. B.; Walden, F. S.; Thomas, R. L.; Gardiner, D. S.; Jacobs, B. W.; Nackashi, D. P.; Damiano, J. *Microscopy and Microanalysis* **2014**, *20*, 1572–1573.

(43) Allard, L. F.; Bigelow, W. C.; Wu, Z.; Overbury, S. H.; Unocic, K. A.; Chi, M.; Carpenter, W. B.; Walden, F. S.; Thomas, R. L.; Gardiner, D. S.; et al., *Microscopy and Microanalysis* **2015**, *21*, 97–98.

(44) Unocic, K. A.; Shin, D.; Unocic, R. R.; Allard, L. F. *Oxidation of Metals* **2017**, *88*, 495–508.

(45) de Jonge, N.; Houben, L.; Dunin-Borkowski, R. E.; Ross, F. M. *Nature Reviews Materials* **2019**, *4*, 61–78.

(46) Bhatia, S. K.; Perlmutter, D. D. *AIChE Journal* **1980**, *26*, 379–386.

(47) Panerai, F.; Martin, A.; Mansour, N. N.; Sepka, S. A.; Lachaud, J. *Journal of Thermophysics and Heat Transfer* **2014**, *27*, 181–190.

(48) Qin, X.; Lu, Y.; Xiao, H.; Wen, Y.; Yu, T. *Carbon* **2012**, *50*, 4459 – 4469.

(49) Takaku, A.; Shioya, M. *Journal of Materials Science* **1990**, *25*, 4873–4879.

(50) Gupta, A.; Harrison, I. R.; Lahijani, J. *Journal of Applied Crystallography* **1994**, *27*, 627–636.

(51) Frank, F. C.; Johnson, D. J.; Watt, W.; Harris, B.; Ham, A. C. *Philosophical Transactions of the Royal Society of London. Series A, Mathematical and Physical Sciences* **1980**, *294*, 443–449.

(52) Guigon, M.; Oberlin, A.; Desarmot, G. *Fibre Science and Technology* **1984**, *20*, 55 – 72.

(53) Bennett, S.; Johnson, D. *Carbon* **1979**, *17*, 25 – 39.

(54) Perret, R.; Ruland, W. *Journal of Applied Crystallography* **1970**, *3*, 525–532.

(55) Edie, D. D. *Carbon* **1998**, *36*, 345–362.

(56) Johnson, D. J. *Journal of Physics D: Applied Physics* **1987**, *20*, 286–291.

(57) Kinoshita, K. **1988**,

(58) Jonge, N. d.; Peckys, D. B.; Kremers, G. J.; Piston, D. W. *Proceedings of the National Academy of Sciences* **2009**, *106*, 2159–2164.

(59) Sacci, R. L.; Black, J. M.; Balke, N.; Dudney, N. J.; More, K. L.; Unocic, R. R. *Nano Letters* **2015**, *15*, 2011–2018, PMID: 25706693.

(60) Tandon, D.; Hippo, E.; Marsh, H.; Sebok, E. *Carbon* **1997**, *35*, 35 – 44.

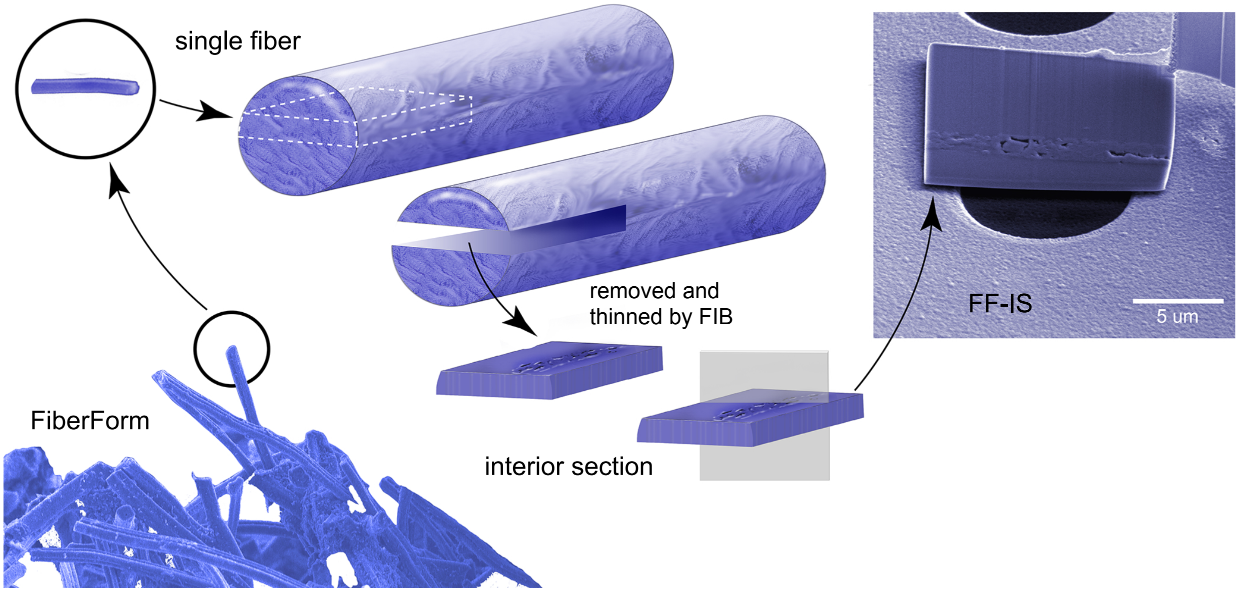

Figure 1: Schematic showing the orientation of the specimen, FF-IS, that was removed and sectioned from within a single FiberForm fiber then placed on a Protochip E-chip within the Atmosphere holder.

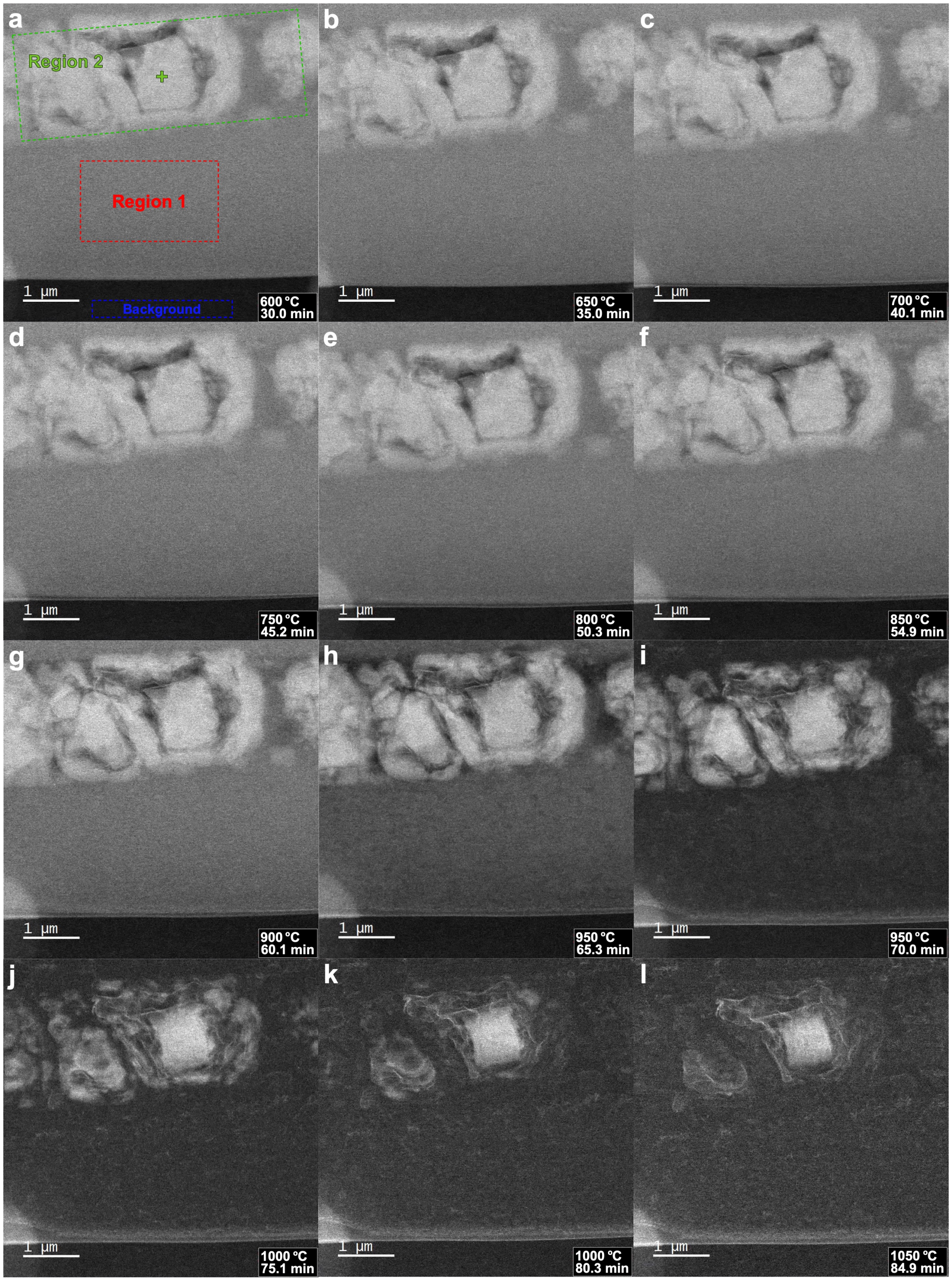

Figure 2: A series of ADF STEM images of FF-IS during oxidation with experiment time and temperature noted on images. Region 1 (red box) is defined as the uniform carbon area of FF-IS, Region 2 (green box) represents the FiberForm inclusion and the background (blue box) is the bottom region with no specimen covering the Si_xN_x window.

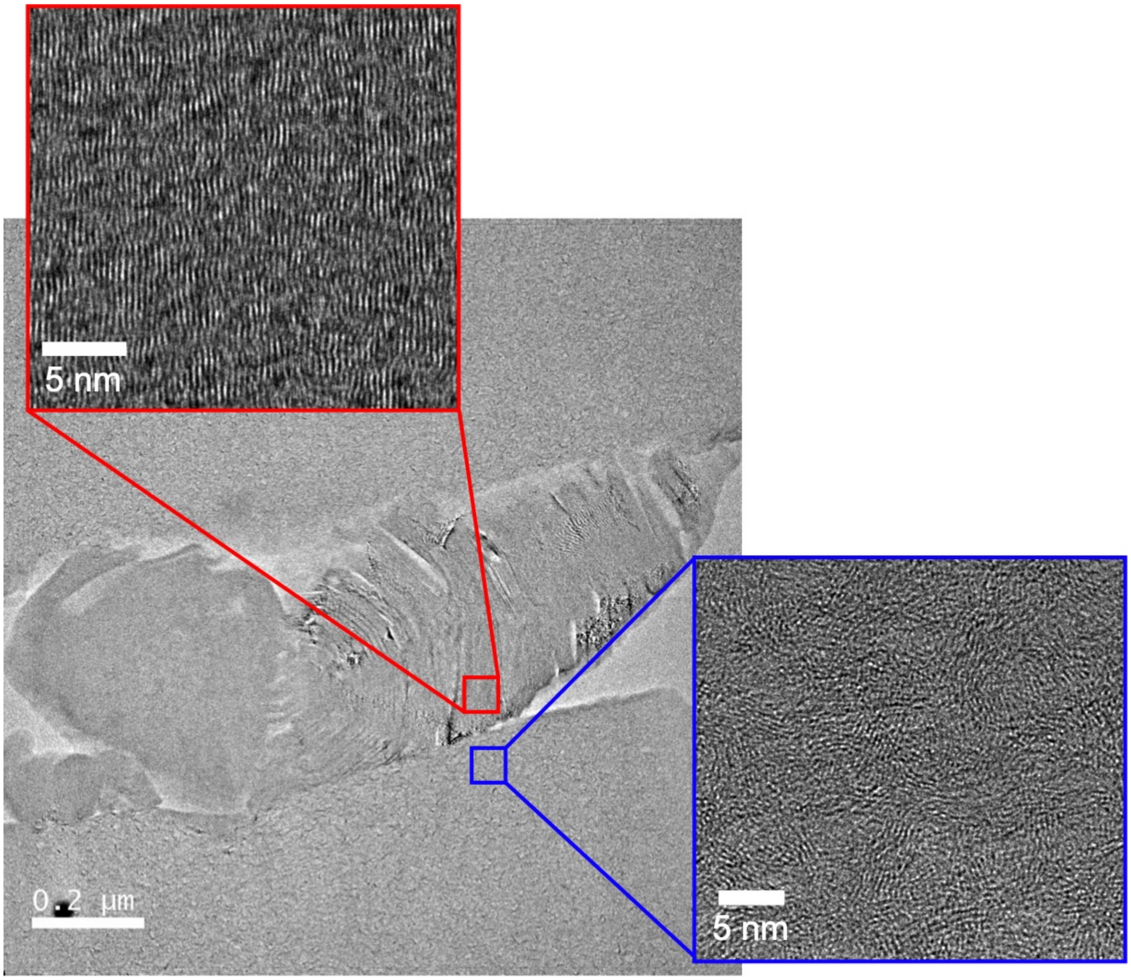

Figure 3: HRTEM images prior to oxidation of comparable FiberForm specimen with microstructures similar to the regions in FF-IS.

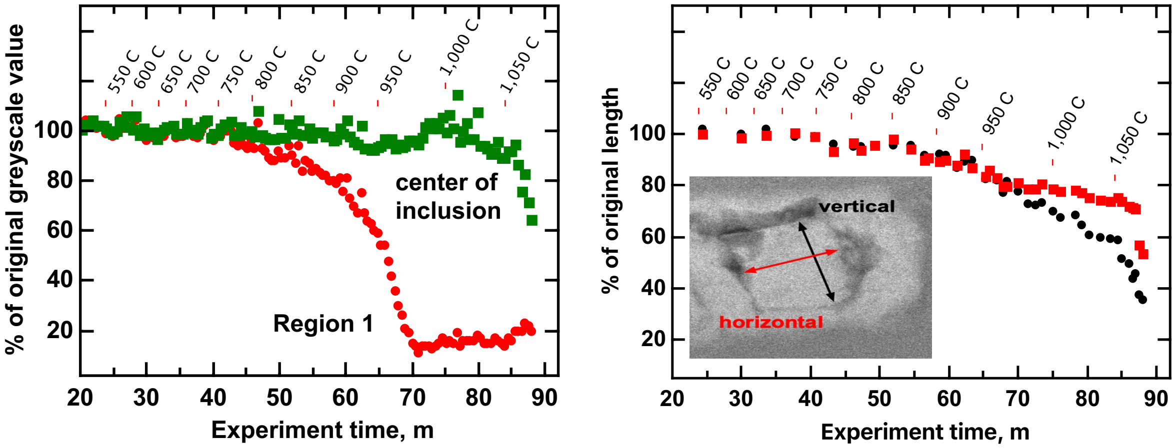

(a)

(b)

Figure 4: (a) Grey-scale values of Region 1 (red circles) and the center of the square inclusion particle (green squares) normalized by the background value as a function of experiment time. The time at which the temperature was increased is shown above by red marks. Regions are illustrated in Fig. 2a; (b) Vertical and horizontal measurements of a single inclusion particle during oxidation of FF-IS as a function of experiment time. The time at which the temperature was increased is shown above by red marks.

Table of Contents Graphic

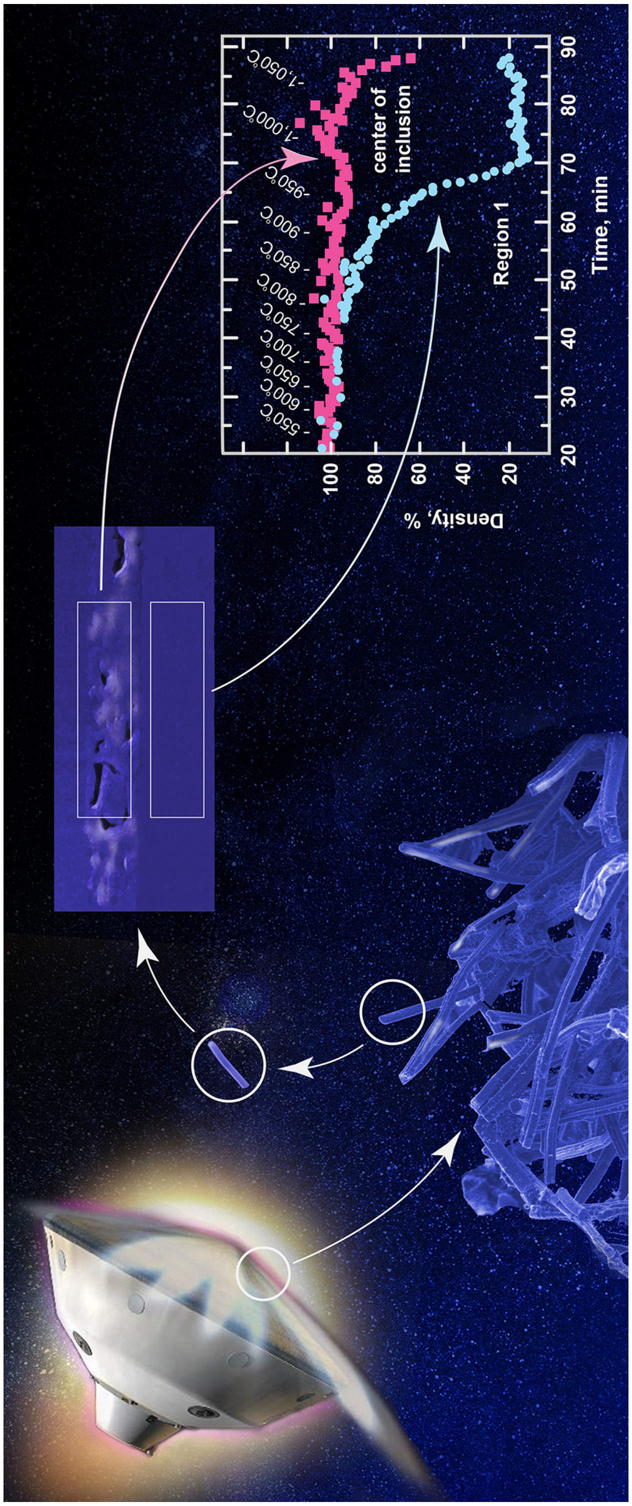

Supporting Information

Structural voids

Detailed view of the needle-shaped voids shown in Fig. 3, oriented vertically and parallel with the lattice fringes. The voids are present between ribbons in the structure, close to where the carbon folds over on itself.

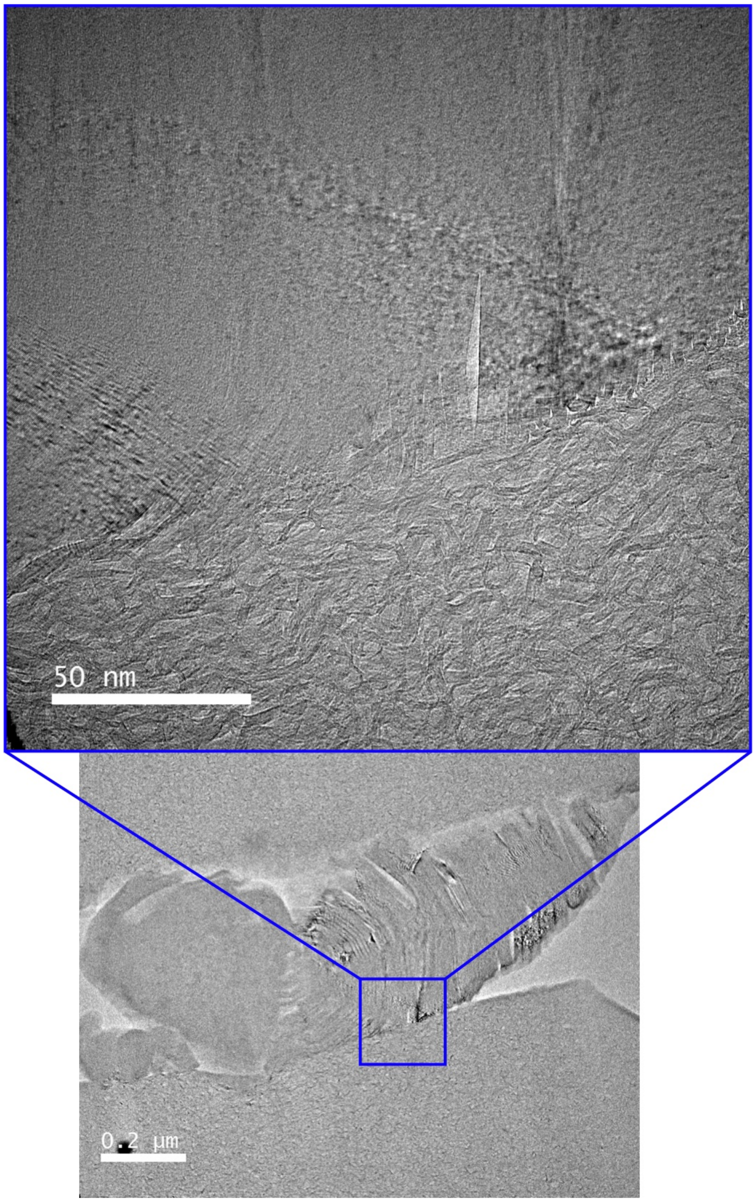

Figure 5: HRTEM images of the area shown in Fig. 3.

SEM image

SEM images from another FiberForm specimen and E-chip before and after a similar oxidation experiment show that only the Si_xN_y window with a FiberForm specimen on top undergoes noticeable differences in appearance (Fig. 6 of the Supporting Information), suggesting that the change is the result of deposition of oxidation products or tungsten impurities from the FIB transfer procedure and not an oxidation of the Si_xN_y material.

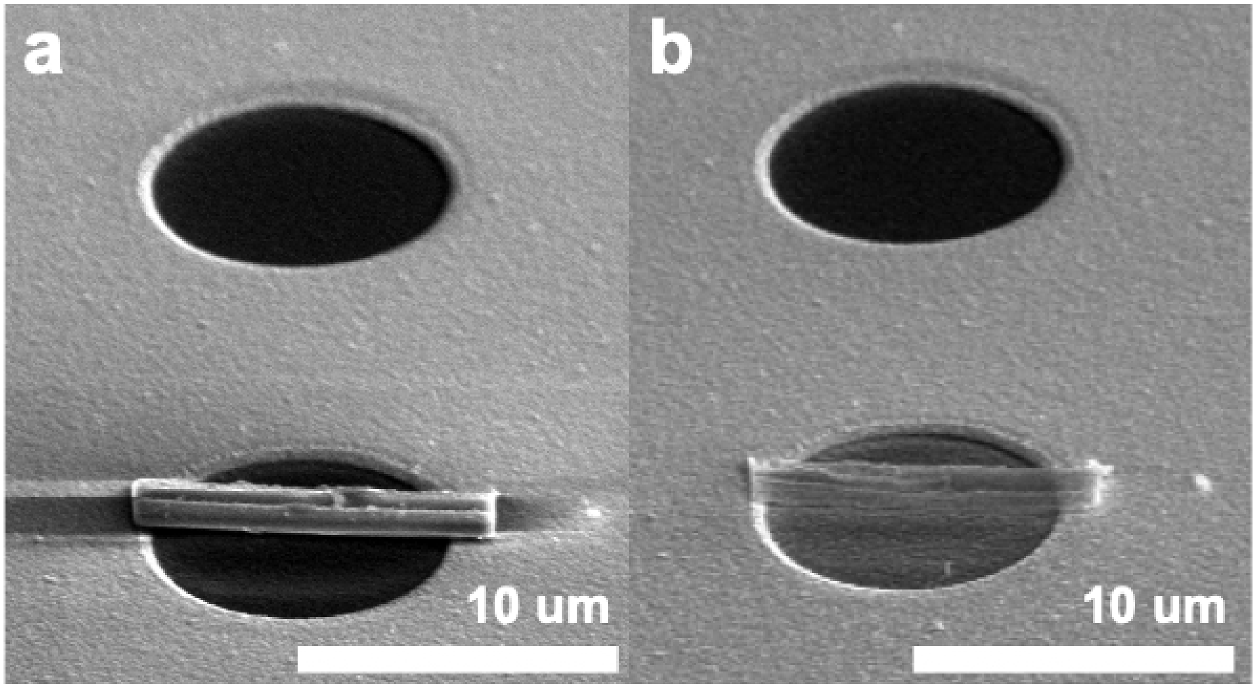

Figure 6: SEM images of a FiberForm specimen and E-chip (a) before and (b) after undergoing a similar oxidation experiment as FF-IS.

XRD analysis of residue

X-ray diffraction (XRD) of the white deposits present in Region 1 (Fig. 2i-l), showing to be a mixture of calcium oxide and calcium silicate. Powders of FiberForm and the oxidized residue were scanned with a Siemens D5000 X-ray Diffractometer using a Cu K_α radiation source in steps of 0.02°.

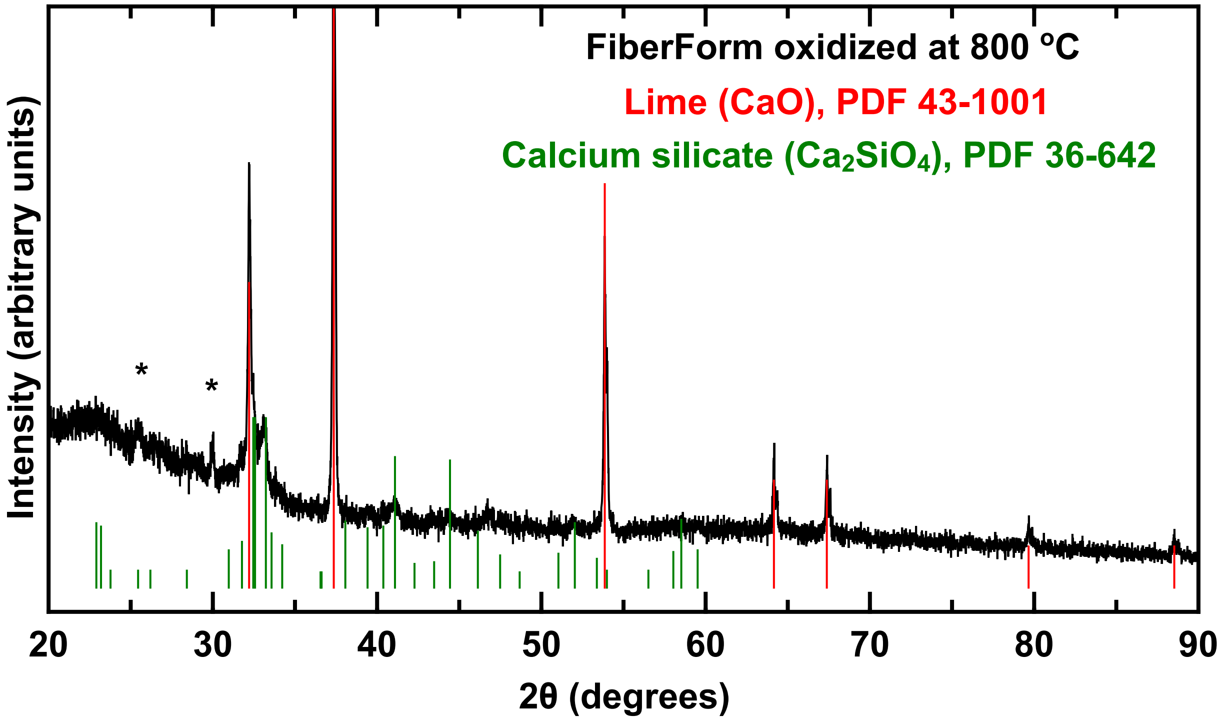

Figure 7: XRD scan of FiberForm® oxidized at 800°C in a box furnace until only a white residue remained. The ⋆ indicates unidentified peaks.